# The Heartbeat of the Oligocene Climate System

Heiko Pälike, *et al.*

*Science* **314**, 1894 (2006);
DOI: 10.1126/science.1133822



Science (print ISSN 0036-8075; online ISSN 1095-9203) is published weekly, except the last week in December, by the American Association for the Advancement of Science, 1200 New York Avenue NW, Washington, DC 20005. 

# The Heartbeat of the Oligocene Climate System

Heiko Pälike,[1*] Richard D. Norris,[2] Jens O. Herrle,[1,3] Paul A. Wilson,[1] Helen K. Coxall,[4] Caroline H. Lear,[4] Nicholas J. Shackleton,[5†] Aradhna K. Tripati,[5] Bridget S. Wade[6]

A 13-million-year continuous record of Oligocene climate from the equatorial Pacific reveals a pronounced "heartbeat" in the global carbon cycle and periodicity of glaciations. This heartbeat consists of 405,000-, 127,000-, and 96,000-year eccentricity cycles and 1.2-million-year obliquity cycles in periodically recurring glacial and carbon cycle events. That climate system response to intricate orbital variations suggests a fundamental interaction of the carbon cycle, solar forcing, and glacial events. Box modeling shows that the interaction of the carbon cycle and solar forcing modulates deep ocean acidity as well as the production and burial of global biomass. The pronounced 405,000-year eccentricity cycle is amplified by the long residence time of carbon in the oceans.

Attempts to understand Quaternary glacial-interglacial changes in ice volume and temperature have shown that the coupling between external forcings, the carbon cycle, atmospheric greenhouse gas concentrations, and glaciations is extremely complex. Nevertheless, records from the past few hundred thousand years indicate that glaciations lag changes in the carbon cycle and orbital forcing (*1*). An insight into the mechanisms that link these three elements of the Earth system is crucial to successfully modeling past and future climates accurately. A good understanding of the carbon cycle response to external forcing requires data series several times longer than the longest orbital variations, which are on the order of millions of years and which we show here are an important feature of climatic records during the Oligocene.

Although geologically older periods experienced the most prominent transient climatic events during the Cenozoic [(the past ~65 million years (My)] (*2*), records and analyses of high enough resolution and fidelity to provide data of astronomically directed climate variations over longer intervals of Earth's history are rare. The Oligocene is of particular interest because it represents an early "icehouse" epoch that is thought to have commenced with the initiation of large ice sheets on Antarctica (*3*), experienced extensive variations of sea level (*4*, *5*), and culminated in a major transient glaciation across the Oligocene-Miocene (O-M) boundary [(~23 million years ago (Ma)] (*6*).

**Site 1218 Oligocene stable isotope records.** Here we present a high-resolution [5 to 10 cm, ~4-thousand-year (ky) interval)] climate proxy record (*7*–*9*) spanning the entire Oligocene (~23 to 33.9 Ma), incorporating new and recently published (*3*, *5*, *10*, *11*) benthic foraminiferal stable isotope data from Ocean Drilling Program (ODP) Leg 199, Site 1218, equatorial Pacific (8°53.378′N, 135°22.00′W, 4.8-km water depth) (*12*). The 13-My-long record has been astronomically age-calibrated and is used here to explore the influence of Earth's orbital variations on Oligocene climate. In addition, we include previously published stable isotope data from planktonic foraminifera (*5*) and new bulk sediment stable isotope and $CaCO_3$ (*13*) data along a high-resolution composite depth scale (*14*) (fig. S2). The ODP Leg 199 records are complemented by an uninterrupted set of well-defined geomagnetic reversals across the Oligocene, as well as detailed calcareous and siliceous biostratigraphic datum events (*12*, *14*, *15*).

Foraminiferal stable isotope measurements are controlled by a number of processes, including changes in dominant deep-water masses, ocean circulation, and paleoproductivity, which vary between regions. No single site can represent whole ocean conditions; nevertheless, proxy records from the deep Pacific ocean can be regarded as those most closely resembling globally averaged temperature and ice-volume conditions because of the large size of the Pacific reservoir and its isolation from surface temperature variations. The data set from Site 1218 provides a means to tie future records to this high-resolution archive in order to develop a more global proxy record and to further assess the potential role of substantial changes in ocean circulation, for example, in response to opening Southern Ocean gateways and closure of the Tethys Ocean.

The basis of our astronomical age model is a new orbital integration (*16*) that has been shown (*17*) to fit geological data, specifically the past 30 My, better than a previous solution (*18*), by using present-day values for the dissipative Earth model (*19*). Building on the shipboard stratigraphy (*12*), an initial astronomical age model was generated from physical property proxy records reflecting the percentage of $CaCO_3$ contents (*14*). This initial age model was then improved using the stable isotope measurements. The astronomically calibrated age for the O-M boundary [~23 Ma, as recognized in studies of *Sphenolithus delphix* (*20*) and magnetostratigraphy (*21*, *14*)] agrees well with independently calibrated ages for this boundary (*22*–*24*), if adjusted to the new astronomical solution.

Our new single-site Oligocene data set from ODP Site 1218 is presented against astronomical age in Fig. 1. The composite record displays features on temporal scales from thousands to millions of years, chiefly (i) two large-scale glaciation events bracketing the Oligocene, (ii) substantial longer-term (multi-My) secular changes, and (iii) a striking rhythm corresponding to Earth orbital variations, including lead-lag relationships and the time-evolutive behavior of cycle amplitudes. In this study, we use the term "heartbeat of the Oligocene" for three main observations in the data: (i) a persistent 405-ky eccentricity pacing of the carbon cycle as indicated by benthic $\delta^{13}C$, (ii) intervals of recurring "glacial" episodes that broadly follow the ~1.2-My-long amplitude modulation of Earth's obliquity, and (iii) higher-amplitude $\delta^{18}O$ variations during individual short and long eccentricity minima.

Two previously described large transient glaciation events are known as Oi-1 (*4*, *25*) immediately after the Eocene-Oligocene (E-O) boundary (*3*, *26*), and Mi-1 at the O-M boundary (*6*, *22*, *24*, *27*). Under a recent astronomical naming scheme based on the 405-ky cycle of Earth's eccentricity (*5*), these two events correspond to cycles $84_{\text{Eo-C13n}}$ (Oi-1) and $58_{\text{Ol-C6Cn}}$ (Mi-1) (*28*). Within cycle $67_{\text{Ol-C9n}}$, the data show a period of coldest temperatures and/or largest ice volumes during the Oligocene. The transition into the Oligocene icehouse world, represented by a rapid increase in benthic $\delta^{18}O$ and $\delta^{13}C$, commenced around cycle $85_{\text{Eo-C13r}}$. It has been shown to have occurred in a stepwise manner (*3*) and was followed by a ~0.4- to 0.8-My-long recovery phase of decreasing $\delta^{18}O$ and $\delta^{13}C$ to values representative for the early Oligocene. This recovery likely represents a readjustment response of the carbon cycle to the rapid deepening of the oceanic carbonate compensation depth (*3*), well illustrated by bulk (fig. S2) and benthic carbon isotope measurements (Fig. 1C).

At the O-M boundary, we observe an increase of $\delta^{18}O$ values by 0.7 to 0.9 per mil (‰),

[1]National Oceanography Centre, Southampton, School of Ocean and Earth Science, European Way, Southampton SO14 3ZH, UK. [2]Scripps Institution of Oceanography, University of California at San Diego, 308 Vaughn Hall, La Jolla, CA 92093–0244, USA. [3]Department of Earth and Atmospheric Sciences, University of Alberta, 1–26 Earth Sciences Building, Edmonton, AB, T6G 2E3, Canada. [4]School of Earth, Ocean and Planetary Sciences, Cardiff University, Main Building, Park Place, Cardiff CF10 3AT, UK. [5]Department of Earth Sciences, University of Cambridge, Downing Street, Cambridge CB2 3EQ, UK. [6]Institute of Marine and Coastal Science, Rutgers, State University of New Jersey, 71 Dudley Road, New Brunswick, NJ 08901–8521, USA.

*To whom correspondence should be addressed. E-mail: H.Palike@soton.ac.uk

†Deceased (24 January 2006).

comparable with records from other ocean basins, and with similar absolute values as those from the subantarctic Southern Ocean (*22*). Benthic $\delta^{13}C$ increases rapidly during cycle $58_{Oi\text{-}C6Cn}$ (Mi-1) but with a preceding 1- to 2-My trend toward heavier values before the Miocene. Although both transient events, Oi-1 and Mi-1, have clear climatic and paleoceanographic importance (*2*, *3*), the intervening variation and longer-term (multi-My) trends in stable isotope records are of equal interest, and indeed are notable.

The Site 1218 time series show clear oscillations, with typical amplitudes of 0.5 to 1.0‰ in $\delta^{18}O$ and $\delta^{13}C$, at periods related to the Earth's orbital evolution. These oscillations are superimposed on longer term (multi-My) changes throughout the Oligocene that prompt us to recognize at least four distinct phases of the Oligocene (Fig. 1): The first ~2.5 My of the Oligocene (Phase I) are initiated by cycle $84_{Eo\text{-}C13n}$ and constitute the Oi-1 recovery phase. This phase is characterized by a smaller amplitude of Earth's orbital imprint and by the subsequent establishment of longer-term climatic oscillations with a clear 405-ky pattern, typical of the Oligocene, particularly in benthic $\delta^{13}C$, in response to orbital forcing. After the initial 2.5 My of Oligocene time, during Phase II, $\delta^{13}C$ briefly exhibits a minimum of ~0.5‰, followed by a positive excursion and succeeded by a 2-My-long $\delta^{13}C$ decrease to close to 0‰ within cycle $73_{Oi\text{-}C10rn}$. During this phase, $\delta^{18}O$ values show increased variability at higher frequencies in the Milankovitch band. Once this pattern is established, the stable isotope variations continue along a similar baseline for a further 2.5 My during Phase III, albeit with strong orbital scale variations, following Earth's 405-ky eccentricity cycle. Within cycle 67, equatorial Pacific benthic $\delta^{18}O$ reaches peak maximum values (*29*). During Phase IV, $\delta^{13}C$ displays high-amplitude 405-ky cyclicity, whereas $\delta^{18}O$ undergoes a distinct longer-term trend toward increasingly light values over ~1.2 to 2.4 My, with peak warmth at this location, or minimum ice volume, around magnetic polarity chron C6Cr. This feature is also shown in data from the equatorial Atlantic (ODP Leg 154, fig. S3). Phase IV culminates with the transient glacial event Mi-1, during cycle $58_{Oi\text{-}C6Cn}$, which marks the onset of a period of strong and rapid early Miocene climate variability (*6*, *22*).

Our carbonate content and mass accumulation rate determinations (fig. S2) partly reflect the evolution of the stable isotope records, for example, the rapid increase of carbonate content across cycle $84_{Eo\text{-}C13n}$ at ~33.9 Ma, a subsequent overshoot (*3*), and maximum carbonate content during the coldest middle Oligocene, within cycle 67. During the middle Oligocene cold phase, $\delta^{18}O$ reaches heavier values than during either the Oi-1 or Mi-1 events. This observation points to two possible scenarios: Either the record at Site 1218 is not a perfect recorder of global carbon cycle dynamics, temperature, and ice volume, or there are additional factors that influence the overall evolution of climate, independent of the detailed orbital configuration, such as weathering patterns, deep water mass reorganization, and tectonic processes.

The pattern of orbital-scale oscillations superimposed on multi-My trends in the Site 1218 stable isotope record reveals an Earth system that appears sensitive to Earth's orbital variations (*3*, *5*, *6*). First, there is a very clear imprint in the benthic isotope series of the long (405 ky) Earth eccentricity variation, particularly in the $\delta^{13}C$ record. Second, the $\delta^{18}O$ record exhibits strong variability at the shorter eccentricity periods (126 and 96 ky). $\delta^{18}O$ also shows correspondence of high isotopic values during periods of low-obliquity amplitude variations, except during cycles 63/64 and 78/79. Oi-1 experiences a temporal delay with respect to low-obliquity amplitude that is presumably related to the initial establishment of large ice volumes on Antarctica. This observation was made previously during the middle Oligocene (*5*) and the Mi-1 event (*6*). The observed pattern correlates the most extreme $\delta^{18}O$ events with low-amplitude obliquity variations (marked in Fig. 1), and minimum eccentricity (a near circular orbit). This pattern is important in that these Oi- glacial events (*4*) have been correlated with sequence stratigraphic studies to estimate magnitudes of eustatic

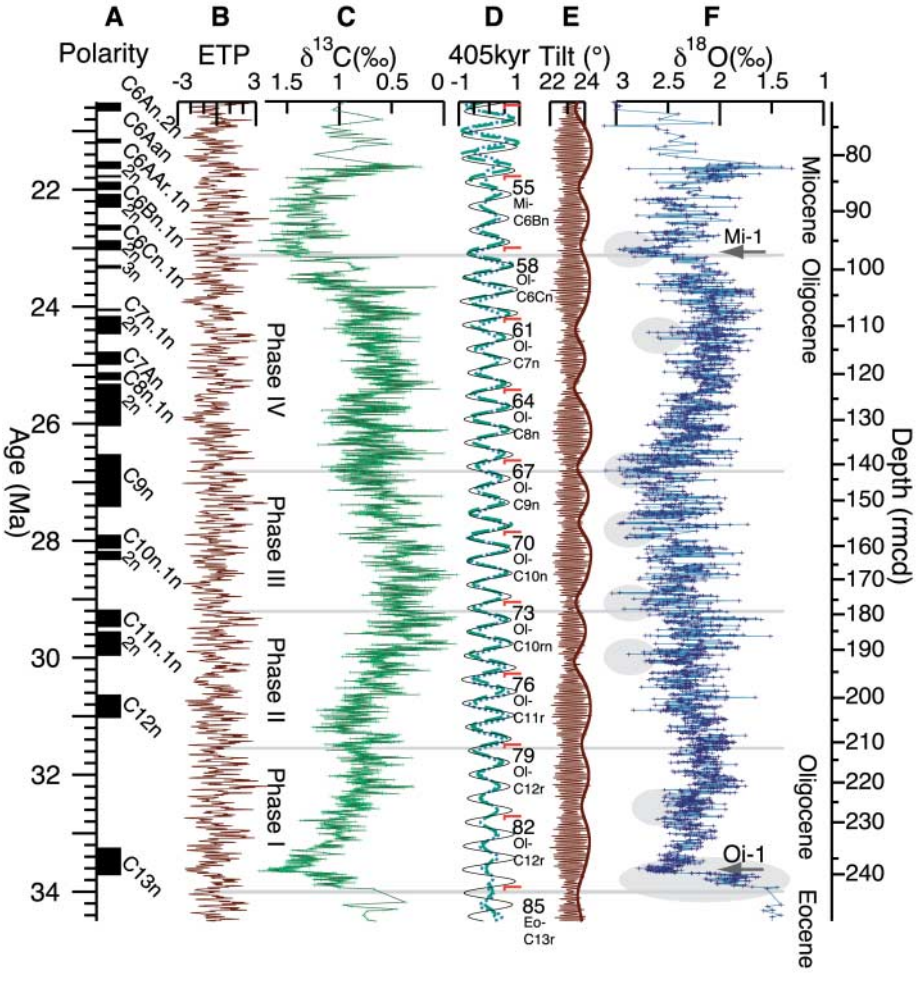


**Fig. 1.** Oligocene Pacific benthic stable isotope data from ODP Site 1218. (**A**) Astronomically age-calibrated magnetic polarity record for Leg 199, based on (*12*, *14*, *15*, *21*). (**B**) Calculated normalized mix of the orbital parameters eccentricity, obliquity (tilt), and climatic precession [ETP, devised in (*40*)], using (*16*). (**C**) Benthic carbon isotope measurement from foraminiferal calcite. (**D**) Bandpass filtering (*41*) to extract the 405-ky eccentricity component from astronomical eccentricity (solid line), benthic inverted $\delta^{13}C$ isotopes (dashed line), and benthic inverted $\delta^{18}O$ isotopes (dotted line). Values close to −1 mark near-circular orbits (minimum 405-ky eccentricity). Also marked are absolute 405-ky eccentricity cycle numbers, counted from the present, following the naming scheme of (*5*). (**E**) Obliquity, and obliquity amplitude envelope (in degrees), from (*16*). (**F**) Benthic oxygen isotope measurements from foraminiferal calcite, Site 1218. Foraminiferal isotope measurements were adjusted to seawater equilibrium by adding 0.64‰ (*42*). Mi-1 and Oi-1 isotope events (*2*) are indicated along the core depth axis by arrows. Depth values are revised meters composite depth (rmcd) (*14*). Horizontal lines mark long-term Oligocene phases. Gray ellipses mark maximum $\delta^{18}O$ during low obliquity amplitudes.

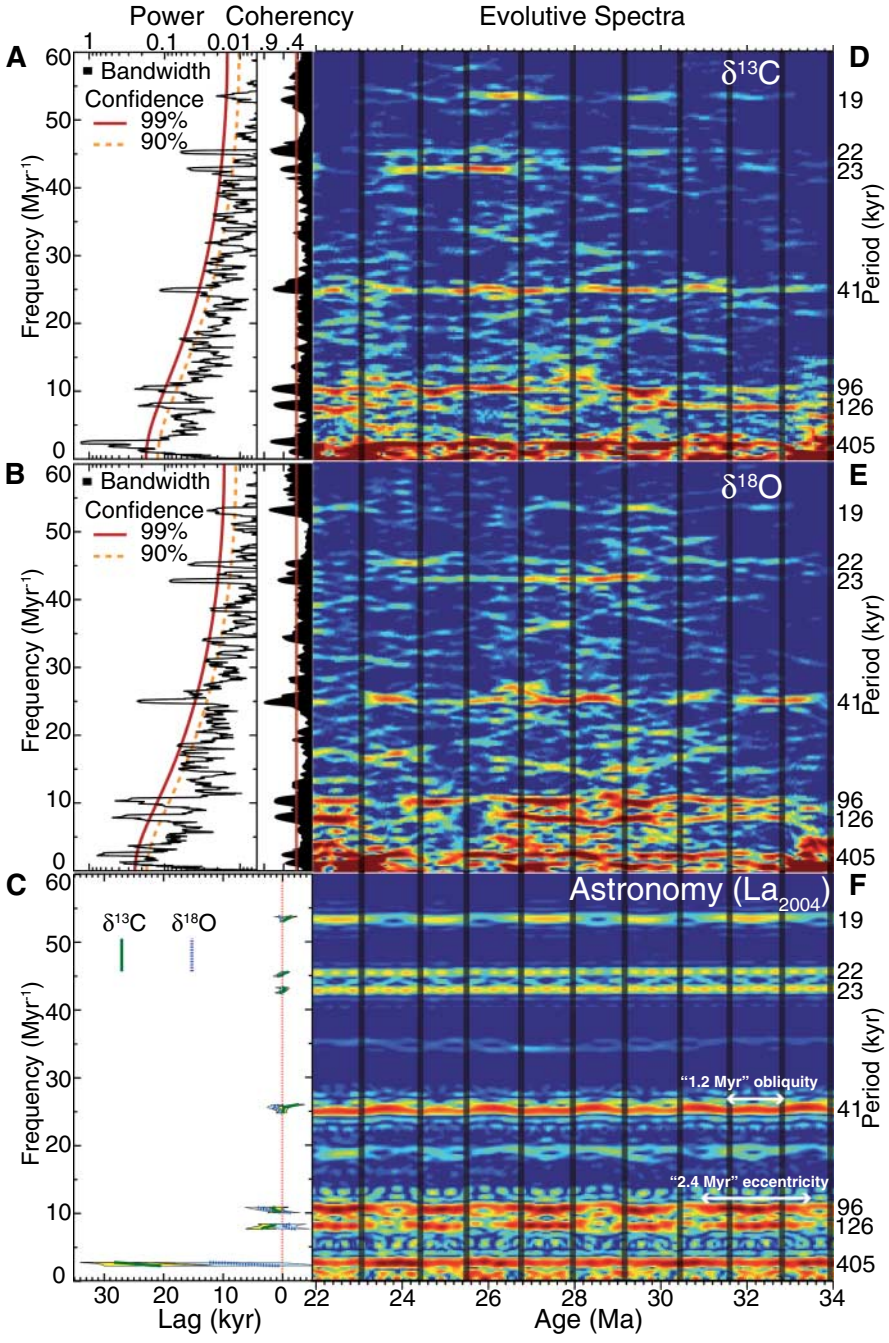


**Fig. 2.** (**A** and **B**) Log-power spectrum of benthic $\delta^{13}C$ and $\delta^{18}O$ time series, determined by the multitaper method (*43*). Before analysis, records were linearly detrended, and a Gaussian notch filter removed periods longer than ~1 My. The time series was interpolated at the average sample resolution (~5 ky).We show coherency estimates between data and astronomical eccentricity, tilt, and precession mix (ETP), using the Blackman-Tukey method, with 280 lags (10% of series from 20.5 to 34.5 Ma). The 99% (solid) and 90% (dashed) confidence levels are shown. $\delta^{13}C$ shows a relatively stronger signal at the longer eccentricity frequencies. (**C**) Blackman-Tukey cross-spectral phase estimates between stable isotopes and ETP curve, converted to lag times in ky (with 95% confidence intervals) (*39*). For climatic precession, obliquity, and short eccentricity, the phase angles are essentially zero. For long eccentricity (405 ky) periods, there is a relative lag of $-\delta^{13}C$ compared with $-\delta^{18}O$ of ~20 ky. (**D** to **F**) Evolutive multitaper method log-power spectra for $-\delta^{13}C$, $\delta^{18}O$, and astronomical ETP showing the temporal evolution of spectral power throughout the Oligocene. Note the correspondence of amplitude variations (high power with hot colors) for the (96 and 126 ky) eccentricity cycles and $\delta^{18}O$, and between the strong 405-ky eccentricity cycle and the 41-ky obliquity cycle between $\delta^{13}C$ and ETP, supporting previous analysis (*17*). Vertical bars mark obliquity amplitude minima every ~1.2 My (also see fig. S2).

Oligocene sea-level variations (*30*), which our data help to constrain. Our extended time series show that the relationship between astronomical patterns and more extreme Oligocene glaciation periods (*5*) holds throughout most of the Oligocene (Fig. 1), with additional events that do not appear to be correlated to astronomical forcing.

**Time series and spectral analysis.** Power spectra for $\delta^{18}O$ and $\delta^{13}C$ (Fig. 2) exhibit peaks at astronomical frequencies that are significantly above 99% confidence estimates using a red-noise model. Our results confirm the observation that both time series exhibit strong power at eccentricity periods (405, 126, and 96 ky). $\delta^{13}C$ shows a stronger response at longer periods (405 ky), whereas $\delta^{18}O$ shows more sensitivity at shorter eccentricity periods (96 and 126 ky). Both records also show a significant response at the main obliquity period (41 ky), with a weaker response at the lower-amplitude obliquity periods (29 and 54 ky). Because of its length, our data set allows us to trace intervals carrying a signal of climatic precession with higher statistical significance than has been possible in previous studies (*3*, *6*).

Phase estimates between astronomy and data (Fig. 2C) determine a ~20 ky lag of $\delta^{13}C$ compared to $\delta^{18}O$ for long eccentricity cycles (405 ky), with close to zero lags for other astronomical terms. Phase estimates between $\delta^{13}C$ compared to $\delta^{18}O$ suggest that $\delta^{13}C$ shows increased lag times for correspondingly longer periods, a behavior that we are able to model as part of this study. A similar pattern has been recognized previously in late Oligocene records (*6*, *22*). This observation is compatible with the long residence time of carbon in the oceans [~0.1 My (*31*)] that transfers energy from climatic precession into eccentricity bands through a nonlinear process, resulting in a frequency-dependent phase lag of $\delta^{13}C$.

We also calculated evolutive spectra for $\delta^{13}C$ (Fig. 2D), $\delta^{18}O$ (Fig. 2E), and astronomical time series [Fig. 2F, (*16*)]. Our results reveal a consistent imprint of the eccentricity and obliquity signals in the $\delta^{18}O$ record, following closely the amplitude modulation terms that coincide with most of the Oligocene glacial events (*5*), including events around cycle $58_{Ol\text{-}C6Cn}$ (~23 Ma) (*6*). The ~2.4-My modulation of the 96- and 126-ky eccentricity cycles is notably similar in the astronomy and in $\delta^{18}O$. All three precession frequencies intermittently appear in the evolutive spectra, and for $\delta^{18}O$ the 19-ky amplitude variation follows the predictions of calculated eccentricity. The strength of the climatic precession traces are at least partially related to higher sedimentation rates, with more consistent responses where sample resolution is higher, mostly ~24 to 27 Ma. However, during the earliest part of the record (*3*), the response to climatic precession is weak, despite higher mass accumulation rates that occurred after the dramatic shift in the depth of carbonate compensation (*3*, *32*).

**Box modeling results.** A previous modeling study that focused on the E-O transition found that an imposed astronomical forcing has a considerable effect on the Earth's climate system (*33*). Loutre *et al.* (*34*) demonstrate that climatic precession and obliquity are the dominant astronomical periods in insolation calculations that use the traditional Milankovitch summer insolation hypothesis, with only a very minor contribution by Earth's eccentricity periods. Our data for the Oligocene, in contrast, exhibit an unexpectedly strong ~405-ky signal in $\delta^{13}C$ as well as in the carbonate flux. The mismatch between the strongest periodicities in most insolation calculations and the climate system response recorded in our data prompt us to evaluate the response of the carbon cycle to astronomical climate forcing. We do this by using a suite of carbon cycle box models, with the aim to gain a better understanding of how astronomical forcing terms are transferred through the carbon cycle. We modified two previously published carbon cycle box models of varying complexity [Model A (*35*); Model B (*36*)] and combined them with astronomical forcing time series to investigate whether we can qualitatively explain basic features of our data (*37*).

By first applying a white-noise signal as forcing input, we established that fundamental properties of both models are the preferential amplification of lower-frequency components and the attenuation of higher-frequency components, resulting in a red-noise transfer function from model input to output (*37*). In the models used, sea-level variations influence the weathering of silicate rocks directly by changing the land area available for weathering on Antarctica and indirectly through the change of carbonate ion concentration. We currently do not model the influence of sea-level on basin-to-shelf fractionation (*38*) and the deposition of carbonate on shallow shelf areas directly. This process would exert additional positive feedback between sea level and the carbon cycle.

Figure 3 shows the model response to astronomical forcings that are dominated by climatic precession and obliquity. We found that applying astronomical forcing terms to globally averaged temperature alone does not result in a response of both $\delta^{18}O$ and $\delta^{13}C$, as observed in our data. Yet, a good match between model output and our data is achieved by also applying astronomical forcing to key components of the carbon cycle. Specifically, we force the effective solar constant in the model by simultaneously applying scaled annual and boreal (65°N) summer orbital insolation changes. The actual temperature is then calculated as a function of both solar constant and carbon dioxide concentration. Here we use 65°N summer insolation to obtain a representative model response for a larger suite of possible insolation forcings (*34*). The same result could have been achieved by applying a seasonal insolation curve from lower latitudes with a smaller obliquity imprint. For the carbon cycle, we use seasonal insolation to modulate the downward flux of particulate organic matter (loosely termed "productivity"); during warmer climates, this downward flux is reduced.

By forcing both global annual temperature and carbon burial in the model of (*35*) by a synthetic insolation curve, we are able to reproduce the strong ~405-ky cyclicity seen in our $\delta^{13}C$ data. Interestingly, some of our model configurations show that by imposing a gradual decrease in atmospheric $CO_2$ levels some time before the E-O transition, similar to (*33*), we obtain a rapid onset of glaciation at the time that it is observed in our records. We find that onset of glaciation is independent of the exact timing of $CO_2$ reduction and is triggered by astronomical forcing as soon as atmospheric $CO_2$ levels are close to a threshold value. Our model results therefore confirm the view (*33*) that a decrease in atmospheric $CO_2$ is a possible mechanism to explain the record across the E-O transition.

Within the astronomically driven carbon cycle we also investigated the possible response of the oceanic carbonate ion ($CO_3^{2-}$) concentration by combining astronomical forcing terms with the more sophisticated model of (*36*), which includes individual representations of the Atlantic, Indian, and Pacific deep oceans, the thermocline, surface waters, and carbon reservoirs. In this case, we forced global temperature by the annual and mean monthly summer insolation (65°N) and carbon burial by mean monthly summer insolation (Fig. 3C). We are able to reproduce a strong eccentricity-driven response in the modeled lysocline depth (Fig. 3D) from a forcing term that is dominated by climatic precession. The model output matches the first-order features of our sedimentary $CaCO_3$ content record, which we interpret as a proxy for lysocline depth variations on orbital time scales.

**Global carbon cycle implications.** Earth seems to "breathe" on time scales ranging from the annual to the orbital. We hypothesize that in all cases these cycles are driven by the expansion and contraction of biosphere productivity in response to changes in solar insolation. Our modeling studies show that the main reasons for the strength of the 405-ky cycle in the carbon isotope data appear to be the long residence time of carbon in the oceans amplifying longer forcing periods, as well as a smaller contribution attributable to the dampening effects of dissolution of sea-floor carbonate on the shorter-term forcing. In addition, we find that applying astronomical forcing to key variables of the carbon cycle, rather than to temperature alone, is necessary to model the principal features of our data set, adding strength to the view (*1*) that the effect of orbital forcing is imprinted upon paleoclimatic records through an influence on the carbon cycle as well as temperature.

### References and Notes


1. N. J. Shackleton, *Science* **289**, 1897 (2000).
2. J. C. Zachos, M. Pagani, L. Sloan, E. Thomas, K. Billups, *Science* **292**, 686 (2001).
3. H. K. Coxall, P. A. Wilson, H. Pälike, C. H. Lear, J. Backman, *Nature* **433**, 53 (2005).




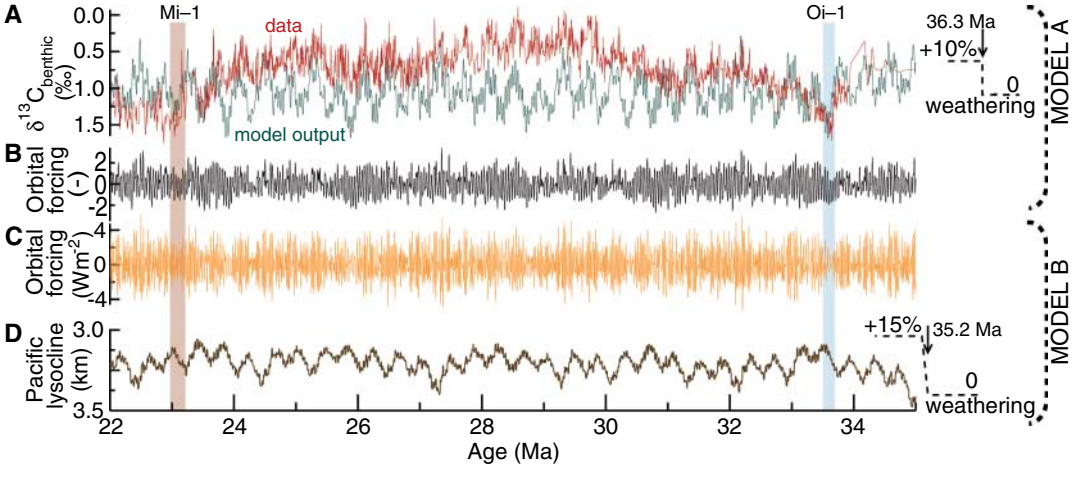


**Fig. 3.** (**A** and **B**) Model A, adapted from (*35*). (**C** and **D**) Model B, adapted from (*35*, *36*). Ages and step functions on right side illustrate change in silicate weathering applied to both models to simulate the onset of the Oligocene icehouse. (A) $\delta^{13}C$ data and model A output. Note the close correspondence between model and data at the 405-ky eccentricity period. (B) Orbital forcing applied to Model A. This forcing is dominated by obliquity, with smaller contributions from eccentricity and climatic precession. (C) Main summer insolation (65°N, June and July) forcing applied to Model B. (D) Pacific lysocline depth variations from Model B. Note strong 405-ky cyclicity compared with forcing (C).

4. K. G. Miller, J. D. Wright, R. G. Fairbanks, *J. Geophys. Res. Sol. Earth Planets* **96**, 6829 (1991).
5. B. S. Wade, H. Pälike, *Paleoceanography* **19**, PA4019 (2004).
6. J. C. Zachos, N. J. Shackleton, J. S. Revenaugh, H. Pälike, B. P. Flower, *Science* **292**, 274 (2001).
7. Our detailed Oligocene Pacific data set is available in electronic form at a designated data repository (www.pangaea.de). Accession codes are http://doi.pangaea.de/10.1594/PANGAEA.547942, http://doi.pangaea.de/10.1594/PANGAEA.547798, and http://doi.pangaea.de/10.1594/PANGAEA.547800.
8. Data were generated in five laboratories. A lower-resolution record across the entire interval (*10*) shows that there are no discernible interlaboratory offsets.
9. Methods are available as supporting material on *Science* Online.
10. C. H. Lear, Y. Rosenthal, H. K. Coxall, P. A. Wilson, *Paleoceanography* **19**, PA4015 (2004).
11. A. Tripati, H. Elderfield, L. Booth, J. Zachos, P. Ferretti, *Sci. Res., Proc. Ocean Drill. Prog.* (Ocean Drilling Program, College Station, TX, 2006), vol. 199.
12. M. Lyle *et al.*, *Init. Rep., Proc. Ocean Drill. Prog.* (Ocean Drilling Program, College Station, TX, 2002), vol. 199.
13. Measured $CaCO_3$ content was used to calibrate calculated $CaCO_3$ from physical property measurements (*12*).
14. H. Pälike *et al.*, *Sci. Res., Proc. Ocean Drill. Prog.* (Ocean Drilling Program, College Station, TX, 2005), vol. 199.
15. L. Lanci, J. M. Parés, J. E. T. Channell, D. V. Kent, *Earth Planet. Sci. Lett.* **237**, 617 (2005).
16. J. Laskar *et al.*, *Astron. Astrophys.* **428**, 261 (2004).
17. H. Pälike, J. Laskar, N. J. Shackleton, *Geology* **32**, 929 (2004).
18. J. Laskar, F. Joutel, F. Boudin, *Astron. Astrophys.* **270**, 522 (1993).
19. H. Pälike, N. J. Shackleton, *Earth Planet. Sci. Lett.* **182**, 1 (2000).
20. I. Raffi, *Phil. Trans. R. Soc. London Ser. A* **357**, 1975 (1999).
21. L. Lanci, J. M. Parés, J. E. T. Channell, D. V. Kent, *Earth Planet. Sci. Lett.* **226**, 207 (2004).
22. K. Billups, H. Pälike, J. E. T. Channell, J. C. Zachos, N. J. Shackleton, *Earth Planet. Sci. Lett.* **224**, 33 (2004).
23. N. J. Shackleton, M. A. Hall, I. Raffi, L. Tauxe, J. Zachos, *Geology* **28**, 447 (2000).
24. H. Pälike, J. Frazier, J. C. Zachos, *Quat. Sci. Rev.*, in press; available online at http://dx.doi.org/10.1016/j.quascirev.2006.02.001.
25. J. P. Kennett, N. J. Shackleton, *Nature* **260**, 513 (1976).
26. J. C. Zachos, T. M. Quinn, K. A. Salamy, *Paleoceanography* **11**, 251 (1996).
27. H. A. Paul, J. C. Zachos, B. P. Flower, A. Tripati, *Paleoceanography* **15**, 471 (2000).
28. The cycle naming scheme (*5*) incorporates the 405-ky cycle number, the geological epoch, and the nearest magnetic polarity chron.
29. S. Van Simaeys, H. Brinkhuis, J. Pross, G. L. Williams, J. C. Zachos, *Geology* **33**, 709 (2005).
30. S. F. Pekar, N. Christie-Blick, M. A. Kominz, K. G. Miller, *Geology* **30**, 903 (2002).
31. W. S. Broecker, T.-H. Peng, *Tracers in the Sea* (LDGO Press, Palisades, NY, 1982).
32. T. H. van Andel, *Earth Planet. Sci. Lett.* **26**, 187 (1975).
33. R. M. DeConto, D. Pollard, *Nature* **421**, 245 (2003).
34. M. F. Loutre, D. Paillard, F. Vimeux, E. Cortijo, *Earth Planet. Sci. Lett.* **221**, 1 (2004).
35. J. C. Zachos, L. R. Kump, *Global Planet. Change* **47**, 51 (2005).
36. J. C. G. Walker, J. F. Kasting, *Palaeogeogr. Palaeoclimatol. Palaeoecol.* **97**, 151 (1992).
37. A description of the modified model equations can be found in (*9*).
38. B. N. Opdyke, J. C. G. Walker, *Geology* **20**, 733 (1992).
39. D. Paillard, L. Labeyrie, P. Yiou, *EOS Transactions AGU* **77**, 379 (1996).
40. J. Imbrie *et al.*, *Milankovitch and Climate, Part 1*, A. L. Berger, *et al.*, Eds. (Reidel, 1984), pp. 269–305.
41. The central bandpass frequency was 2.5 $My^{-1}$, with a bandwidth of ±0.5 $My^{-1}$. Filtering was performed using (*39*).
42. N. J. Shackleton, N. D. Opdyke, *Quat. Res.* **3**, 39 (1973).
43. M. Ghil *et al.*, *Rev. Geophys.* **40**, 3.1 (2002).


44. This research used samples and data provided by the Ocean Drilling Program (ODP). ODP is sponsored by the U.S. National Science Foundation (NSF) and participating countries under the management of Joint Oceanographic Institutions (JOI), Inc. We thank the crew and shipboard scientists of ODP Leg 199, particularly I. Raffi and J. Backman for their biostratigraphy work. We thank L. Kump, J. Zachos, J. Walker, and J. Kasting for providing code and information for their models.


**Supporting Online Material**

www.sciencemag.org/cgi/content/full/314/5807/1894/DC1
Methods
SOM Text
Figs. S1 to S3
Tables S4 to S6
References

14 August 2006; accepted 6 November 2006
10.1126/science.1133822

# Epochal Evolution Shapes the Phylodynamics of Interpandemic Influenza A (H3N2) in Humans

**Katia Koelle,[1,2]*† Sarah Cobey,[1]† Bryan Grenfell,[2,3] Mercedes Pascual[1]**

**Human influenza A (subtype H3N2) is characterized genetically by the limited standing diversity of its hemagglutinin and antigenically by clusters that emerge and replace each other within 2 to 8 years. By introducing an epidemiological model that allows for differences between the genetic and antigenic properties of the virus's hemagglutinin, we show that these patterns can arise from cluster-specific immunity alone. Central to the formulation is a genotype-to-phenotype mapping, based on neutral networks, with antigenic phenotypes, not genotypes, determining the degree of strain cross-immunity. The model parsimoniously explains well-known, as well as previously unremarked, features of interpandemic influenza dynamics and evolution. It captures the observed boom-and-bust pattern of viral evolution, with periods of antigenic stasis during which genetic diversity grows, and with episodic contraction of this diversity during cluster transitions.**

Interpandemic influenza causes substantial morbidity and mortality in humans. Annual winter epidemics yield cumulative attack rates between 10 and 20% for influenza A (subtypes H3N2 and H1N1), and influenza B infections (*1*) and contribute heavily to deaths caused by respiratory infections worldwide. The virus is capable of evading immune recognition through continual antigenic drift of its surface glycoproteins, hemagglutinin (HA) and neuraminidase (NA), complicating long-term control of the disease through vaccination (*2*). An understanding of the ecological and immunological processes driving influenza dynamics and evolution is therefore critical for anticipating and ultimately mitigating the effect of this infectious disease. Here we focus on the phylodynamics (*3*) of H3N2, which has been present worldwide since its pandemic appearance in 1968.

One of the most striking characteristics of influenza A evolution is the limited standing diversity of the HA gene, despite the virus's high mutation rate. This limited diversity is evident in its phylogeny: The tree consists of a long trunk with short side branches that are indicative of high extinction rates of the lineages (*4*) (Fig. 1A). Epidemiological factors that contribute to this pattern include the short infectious period of the host and partial cross-immunity between similar strains (*3*). However, the most detailed model of interpandemic influenza to date suggests that these factors alone cannot account for limited diversity and that temporary strain-transcendent (generalized) immunity is necessary to restrict diversity (*5*).

More recently, differences between the genetic and antigenic evolution of the H3N2 virus's HA glycoprotein have been highlighted (*6*). A key unexplained pattern is that, although genetic change is gradual, antigenic change is punctuated. HA inhibition (HI) assays show that H3N2 sequences fall into groups, or clusters, with unique antigenic properties. Between 1968 and 2003, these clusters emerged and replaced each other within 2 to 8 years, exerting a major influence on vaccine strategy (*2*). Empirical evidence suggests that there is almost complete immunity between strains within a cluster (*7*). In contrast, cross-immunity is as low as 60 to 85% between clusters adjacent in time (*7*, *8*) and is undetectable between temporally distant clus-

[1]Department of Ecology and Evolutionary Biology, 2019 Kraus Natural Science Building, University of Michigan, 830 North University Avenue, Ann Arbor, MI 48109-1048, USA. [2]Center for Infectious Disease Dynamics (CIDD), Department of Biology, 208 Mueller Lab, Eberly College of Science, The Pennsylvania State University (PSU), University Park, PA 16802, USA. [3]Fogarty International Center, National Institutes of Health, Bethesda, MD 20892, USA.

*To whom correspondence should be addressed. E-mail: kkoelle@psu.edu
†These authors contributed equally to this work.